

## FEDSM-ICNMM2010-' \$&+(

### EXPERIMENTAL AND NUMERICAL INVESTIGATIONS OF INLET BOUNDARY CONDITIONS FOR A PROPELLER TURBINE DRAFT TUBE

**Jean-Mathieu GAGNON\***

LAMH: Laboratory of Hydraulic Machinery  
Department of Mechanical Engineering  
Laval University  
Quebec, Quebec G1V 0A6  
Email: jean-mathieu.gagnon.1@ulaval.ca

**Felix FLEMMING**

**First Coauthor**  
Voith Hydro, Inc.,  
760 East Berlin Road,  
York, PA 17408, USA

**Ruixia QIAN**

**Second Coauthor**  
Voith Hydro, Inc.,  
9955 Ave de Catania  
Brossard, Canada, J4Z 3V5

**Claire DESCHENES**

**Third Coauthor**  
LAMH  
Laval University  
Quebec, Quebec G1V 0A6

**Stuart COULSON**

**Fourth Coauthor**  
Voith Hydro, Inc.,  
760 East Berlin Road,  
York, PA 17408, USA

#### ABSTRACT

*The flow at the draft tube inlet of a propeller turbine is investigated via numerical simulations and experimental measurements. Two (2) experimental tools are used in combination to measure the velocity field in this study: 3D-Stereoscopic particles images velocimetry and 2D-laser doppler velocimetry. The numerical simulations are performed with steady RANS as well as URANS with the SST turbulence model. The results show the comparison of the turbulence intensity between experiments and CFD. Further assessment of the draft tube inlet flow is made with LDV to assess the circumferential non-uniformity of the flow. Finally, a complete frequency analysis puts in evidence the helical vortex rope frequency at partial discharge among many other flow phenomena. This study considered three operating points of a propeller axial turbine.*

#### NOMENCLATURE

$\alpha$  Relative guide vane angle =  $\alpha/\alpha_{ref}$  [degree]  
 $\alpha_{ref}$  Guide vane angle at nominal head [degree]  
 $Q_{11}$  Unit flowrate [ $m^3 s^{-1}$ ]  
 $N_{11}$  Unit speed [rpm]  
 $\eta$  Hydraulic efficiency [-]  
 $c_i(t)$  Instantaneous velocity component [ $ms^{-1}$ ]  
 $\langle c_i \rangle$  Phase average velocity component [ $ms^{-1}$ ]  
 $c'_i$  Fluctuating velocity component [ $ms^{-1}$ ]  
 $C_i$  Time average velocity =  $\lim_{T \rightarrow \infty} \frac{1}{T} \int_{t_0}^{t_0+T} c_i dt$  [ $ms^{-1}$ ]  
 $\tilde{c}_i$  Difference between  $C_i$  and  $\langle C \rangle$  [ $ms^{-1}$ ]  
 $T_i$  Turbulence intensity =  $\sqrt{2/3(\overline{c_r^2} + \overline{c_t^2} + \overline{c_z^2})}/C_{ref}$  [-]  
 $c_r, c_t, c_z$  Radial, circumferential and axial velocity components [ $ms^{-1}$ ]  
 $C_{ref}$  Reference velocity =  $Q_{ref}/(\pi R_{ref}^2)$  [ $ms^{-1}$ ]  
 $Q_{ref}$  Measured flow rate at OP [ $m^3 s^{-1}$ ]  
 $R_{ref}$   $R_{throat}$  (at runner crown) [m]

\* Address all correspondence to this author.

$\lambda_2$  Second largest eigenvalue of the velocity gradient tensor  
 $[rads^{-1}]$   
 $f_r$  Runner frequency  $[Hz]$

## INTRODUCTION

With the increasing cost for energy and the demand for green energy, low head hydro power plants become economically more feasible and move into the focus of the industry. Propeller turbines represent one turbine type for low head applications with certain benefits in terms of reduced complexity and therefore price. Common to all classical low head hydro power applications is the importance of the diffuser or draft tube to the total turbine efficiency. For this reason the flow in the draft tube is one of the subjects of extensive experimental and numerical research efforts in the Consortium on Hydraulic Machines at the LAMH, Laval University.

The flow inside the draft tube is strongly turbulent and very challenging for today's numerical methods applied in industry as well as in research. This is caused by the decelerating swirling flow resulting in a completely unsteady flow which is not well captured by standard turbulence modeling approaches such as Reynolds Averaged Navier-Stokes (RANS) simulations. One of the key factors in simulating a draft tube properly is to well define inlet boundary conditions. The focus of the paper is put on experimental measurements and different approaches to investigate flow inlet condition. These simulations include steady as well as unsteady approaches. In detail, comparisons are shown between simulations and utilizing profiles obtained from full machine CFD steady RANS and URANS calculations. The CFD results will then be compared to phase resolved experimental data obtained by LDV at various locations inside the draft tube of the propeller turbine.

## Experimental Methods

LDV and PIV measurements have grown in popularity in the field of hydraulic turbine studies in the past 20 years. These instruments have found no equivalent from their fast, precise and reliable optical operation. Figure 1 shows a clipped view of the propeller turbine with measurement locations. The machine has 6 runner blades and 24 guide vanes. The operating point investigated in this paper are at partial discharge (OP. 1), at nominal condition (OP. 2), and at overload condition (OP. 3).

## Stereoscopic Particles Image Velocimetry System

A stereoscopic PIV system was used to measure the averaged velocity field within two blade passages with the help of an encoder tagging the runner instantaneous position. A vertical light sheet with a thickness of 5mm, created by a Nd:Yag laser delivering 60mJ per pulse was projected to illuminate particles

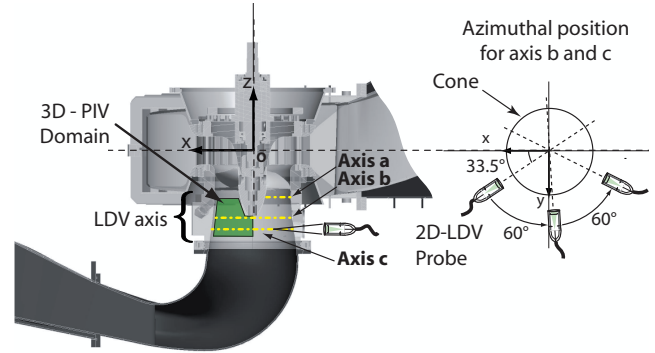


FIGURE 1. Optical access for 2D LDV at runner outlet and PIV domain

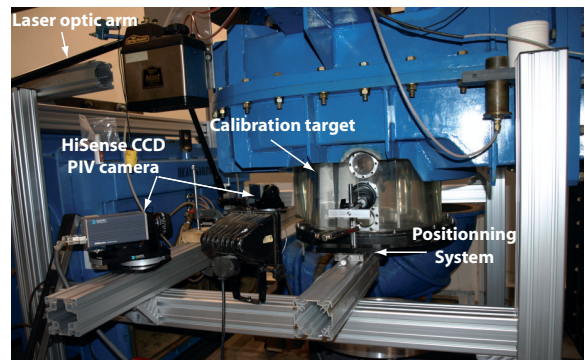
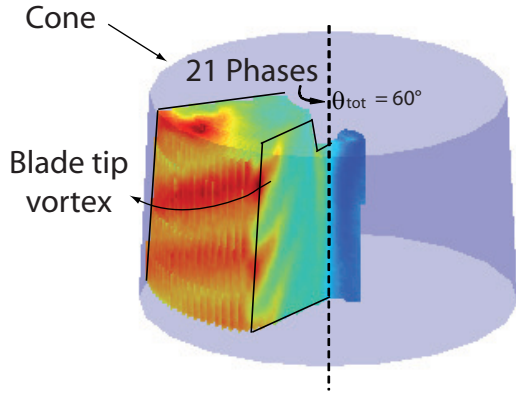


FIGURE 2. 3-D stereoscopic setup on the turbine model

in the cone made of transparent Plexiglas. An optic arm with 6 degrees of freedom was also used to guide the light sheet at the desired position within the cone (Fig. 2). Two HiSense PIV camera with CCD resolution of  $1024 \times 1280$  pixels<sup>2</sup> were installed in an angular displacement configuration and Sheimpflug condition for a best focus on the illuminated particles travelling in the light sheet. The timing between two consecutive pulses was set as low as  $100 \mu s$  to ensure the particles stay within the sheet in the whole spatial domain. This is a requirement from the very wide illuminated zone covering  $0.2 \times 0.150$  m<sup>2</sup> under the cone. For the particles displacement and velocity assessment, an adaptive correlation was implemented starting from 64 pixels interrogation windows with 2 passes and reducing to a final 32 pixels interrogation area. The adaptive correlation helps to minimize loss of pair of particles and gives more good vectors at the end of the processing. Peak and width validation was ensured with median method to remove outliers [1]. Finally, a range validation was performed at the end to remove spurious vectors. This method is similar to histogram clipping.

Velocity fields are phase-averaged on 21 phases (every 3 degrees) with 1000 images per phase to ensure good convergence on statistics. Figure 3 illustrates contours of the phase average



**FIGURE 3.** PIV Phase-averaged circumferential velocity contours under the runner

velocity,  $C_r$ , from PIV measurements in the cone. Dark (or red) shades qualitatively indicate regions of high circumferential velocity evidencing blade tip vortices near the cone wall. Light (or blue) shades expose the velocity deficit from hub and blade wakes.

## 2D Laser Doppler Velocimetry System

A 2D-LDV system with two-components, four-beams, was operated in backscatter on-axis-collection mode. There are two LDA (laser Doppler anemometer) inside the probe head and each LDA uses two laser beams of the same wavelength. For each orthogonal direction, pairs of beams are crossing at the focal point. One pair of beams uses laser wavelengths of  $\lambda = 488.0$  nm (blue) and the other pair uses  $\lambda = 514.5$  nm (green). The probe diameter measures 60 mm with front lens having a focal length of about 400 mm. The measurement volume of the crossing beams is estimated to be  $0.189 \times 0.189 \times 3.97$  mm<sup>3</sup> in size (in air) and there are 36 fringes with  $5.27$   $\mu$ m separation. Bragg-cell shifting at 40 Mhz is used to resolve directional ambiguity. We used a glass window with flat parallel faces for the optical access on the three measurement axis. This results in a small discontinuity with the curved surface inside the cone and the flat window for the optical access. The optical access not used during measurements were filled with a plastic plug perfectly matching the inside geometry to avoid additional disturbance of the flow.

## Signal Analysis

All measurements are phase resolved with an encoder placed on the runner shaft. In the inertial reference frame, the measurements obey the Reynolds triple decomposition with a mean, phase and fluctuating velocity to represent the instantaneous sig-

nal as expressed by Eqn. (1)

$$c_i(t) = \langle c_i \rangle + c_i' = C_i + \tilde{c}_i + c_i' \quad (1)$$

with the phase average velocity defined as,

$$\langle c_i \rangle = C_i + \tilde{c}_i. \quad (2)$$

Where  $C_i$  is the time average velocity,  $\tilde{c}_i$  is the phase average deviation from the time average and  $c_i'$  is the deviation from the phase average coming from the turbulent random motion. Note that the fluctuations are centered around the mean so that  $\overline{\langle c_i \rangle} = \overline{C_i} = C_i$ , where the overline denotes time average.

In LDV measurements, particle velocity is recorded along with the encoder information so we can sort the particles signal with runner angular position,  $\theta_n$ , and average the velocity over a window,  $[\theta_n - \Delta\theta/2, \theta_n + \Delta\theta/2]$ . In this study, we used  $n=720$  discrete angular positions starting at  $\theta = 0.5^\circ$  ( $\Delta\theta = 0.5^\circ$ ). There are 60 000 acquisitions at every measurement location leading to about 80 velocity data per angular position. This amount of data for LDV ensures convergence on statistics.

Any phase averaged quantity,  $\langle \phi \rangle$ , at the angular position,  $\theta_n$ , can now be define with Eqn. 3:

$$\langle \phi_{r_k \theta_n} \rangle = \frac{1}{M} \sum_{j=1}^M \phi_{j r_k \theta_n} \Big|_{\theta_n \pm \Delta\theta/2} \quad n = 1..720 \quad (3)$$

where,  $M$ , represents the number of data points in the evaluation window and subscript,  $j$ , denotes the detected instantaneous quantity within the window. We have added a subscript,  $r_k$ , to represent the  $k$  discrete radial locations where the measurements were taken. There are respectively 12, 40 and 42 radial locations at axis a, b and c giving sufficient resolution to capture most velocity gradients.

For PIV,  $\Delta\theta \simeq 0$  since we can adjust a trigger delay on the laser light pulse and synchronize at the desired runner position with the encoder signal. We assumed the runner angular frequency is constant. Recording were made every 3 degrees with  $n=21$  phases covering 60 degrees of runner rotation or one blade passage. For mean profile against the radius, we merely compute the velocity with a summation over all phase angles

$$\overline{\phi_{r_k}} = \frac{1}{N} \sum_{n=1}^N \langle \phi_{r_k \theta_n} \rangle \quad (4)$$

Where  $N$  is the number of angle locations for PIV, LDV or CFD. As we can see, the same definition applies in simulations with the exception that the resolution of  $\theta$  and  $r$  is given by the mesh resolution and a mass flow average has to be applied in order to account for varying mesh cell sizes.

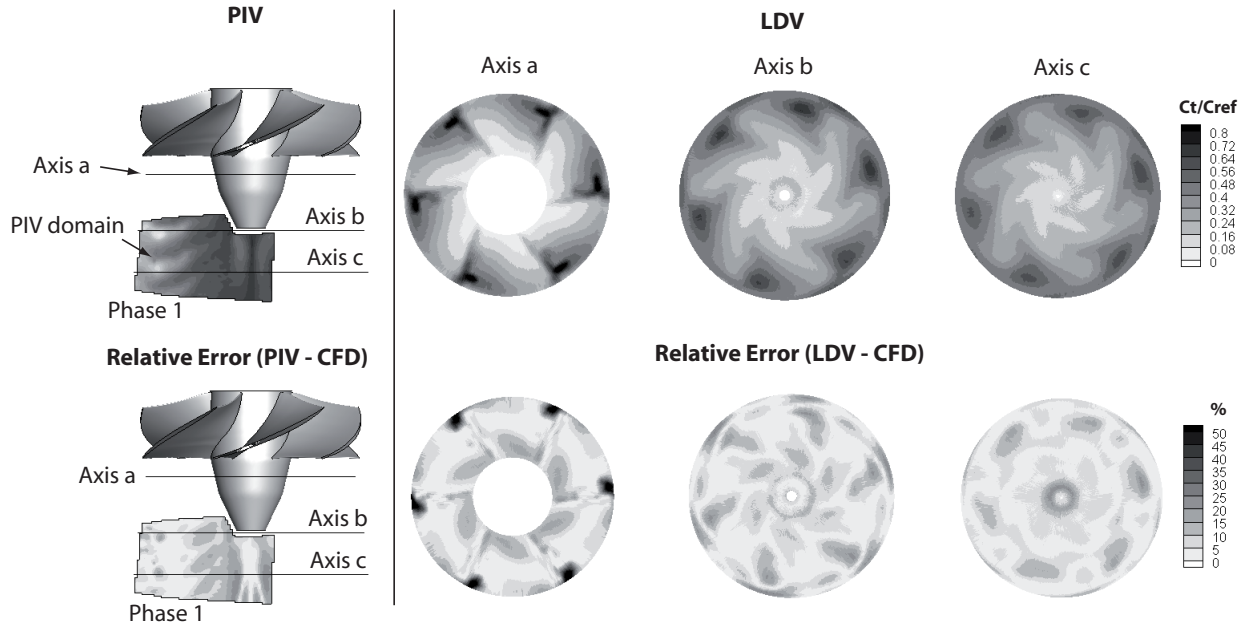


**FIGURE 4.** (Top) Experimental phase average velocity contours of  $C_t/C_{ref}$  at OP. 2 for PIV and PIV, (Bottom) Error contours between experiment and CFD at same operating point

## Numerical Methods

Three types of simulations were used for a complete numerical investigation of the draft tube inlet flow and boundary conditions:

1. Complete machines steady Reynolds averaged Navier-Stokes (RANS) simulations with k- $\epsilon$  turbulence model to obtain the boundary condition for unsteady RANS simulations (URANS). Boundary conditions used were the inlet flowrate and an opening outlet allowing for entrainment.
2. Unsteady simulations of the complete machine without the draft tube elbow using static pressure outlet and the total pressure inlet computed from steady RANS. A SST turbulence model was used for all three operating points.
3. Unsteady draft tube simulations with two different types of inlet boundary conditions to investigate the influence on the recirculation zone in the draft tube cone.

In the steady simulation cases, we used an unstructured mesh whereas all other cases used block structured hexa mesh with refinement at wall boundaries. A steady state torque on runner was achieved after 3 to 7 runner rotations depending on the operating regime of the turbine. Experimental LDV measurement points were recorded during URANS simulations which necessitate over a thousand of monitor points at runner outlet for elevation along lines a, b and c (Fig. 1).

## Validation

To assess how well the simulations represent the flow behavior, a validation of the CFD was made against the experiments at peak condition (OP. 2) for steady simulations (case 1). Figure 4 shows the circumferential phase average velocity,  $C_t/C_{ref}$ , for PIV and also for LDV at axis a, b and c. The phase 1 of the PIV domain is illustrated below the hub on the top left whereas LDV contours are shown on the top three figures of the right.

On the bottom of the figure, the subtraction of the experiment and the simulation data is represented with error contours of the velocity in percentage. The errors between steady CFD and measurements are very small in all locations except for the regions of high circumferential velocity in dark shade clearly visible at axis a, that reach an error of almost 50%. These periodic discrepancies are mainly due to the fact that the blade tip gap was not modeled and the blade was merely elongated up to the shroud for simulations. In this case, the augmentation of circumferential velocity near the shroud cannot be associated with the blade tip vortex generated by leakage effect from pressure to suction side of the blade. In the numerical simulations, the high region of circumferential velocity seems to originate from the blockage effect of a pair of small corner vortices generated by the interaction of the guide vane vortex sheet, the shroud and the blade boundary layers. The contour of  $\lambda_2$  on the left of Fig. 5 shows the development of these small vortex in the chordwise direction from 0% to 100% of the chord length. The guide vanes and the corner vortex are identified respectively by letters g and c standing for the first letter of their name. A contour of  $C_t/C_{ref}$  and an

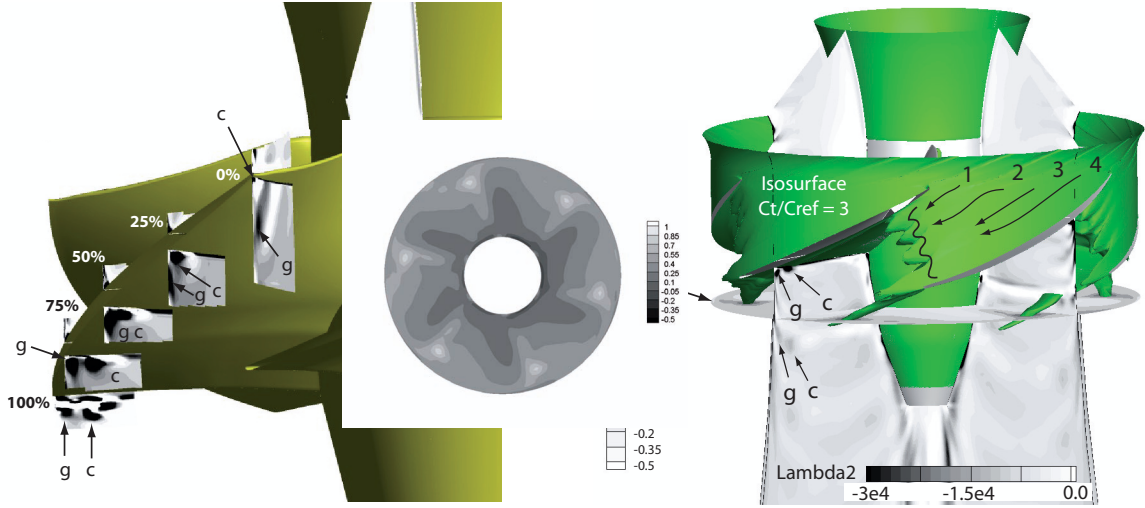


FIGURE 5. (Left) CFD contours of  $\lambda_2$  at OP. 2, (Right) Isosurface of  $C_t/C_{ref}$  and contours of  $\lambda_2$  for steady CFD at OP.2

isosurface at  $C_t/C_{ref} = 3$  on the right figure expose the region of high circumferential velocity just after the vortex core region, at smaller radius. The figure further demonstrates the four guide vanes wakes that are convected downstream with black arrows. The guide vanes vortex sheet standing close to shroud pushes the corner vortex away from the shroud.

In Fig. 6, we use the LDV phase average velocity contour of axis a to get a better view of the global velocity field. It is clear from the velocity profile on the right side of the figure, that the high intensity contour spot seen on the left is the result of the circumferential velocity peak. Conservation of tangential momentum would require a slight augmentation of  $C_t$  in the inter-blade channel to compensate for the combine effect of the blockage and the wall that slow down the flow. The circumferential velocity is further amplified at the trailing edge from the shear layer and the injection of vorticity. Before the blockage at axis a, around  $R/R_{ref} < 0.9$ , the physics of the flow field in the  $C_t$  direction is clearly the one of a solid body rotation seen from the linear increase from hub to shroud ( $R/R_{ref} \sim 0.3$  to 1). The gradient found in the LDV curve, where  $R/R_{ref} \simeq 0.85$  is the difference between the physics of the blade tip gap and the simulation without blade tip. It is surprising that the no gap case mimic the experimental case with a gap.

### Turbulence Intensity

As we have seen, the phase average velocity agrees fairly well and the investigation of other components of velocity, not illustrated here, would show similar error levels. In this subsection, we are concerned about the turbulence quantity from rms values and more closely to the turbulence intensity. Figure 7 shows the results for PIV, LDV and URANS (case 2) at axis c for all operating regimes.

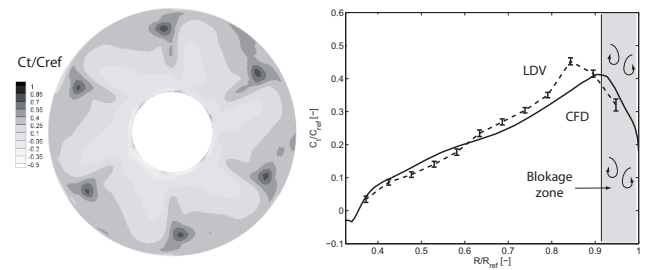
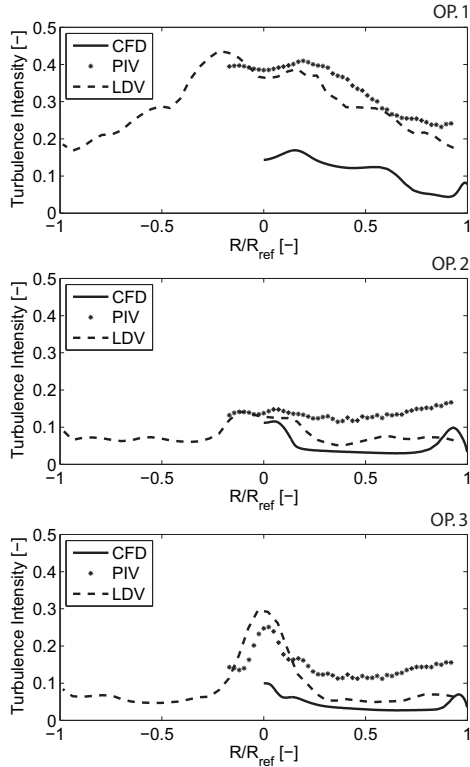


FIGURE 6. (Left) LDV contour of  $C_t/C_{ref}$  at axis a, OP.2, (Right) LDV and steady CFD velocity profile comparison for OP. 2

Even though we have only two orthogonal rms values with the LDV, the turbulence intensity level measured with this instrument is considered to be the reference since it is the most precise. The accuracy of PIV is mainly influenced from the small displacement of the particles in the sheet resulting in large relative uncertainty. Typical subpixel accuracy below 0.1 pixel can be considered for the Dantec software. Figure 8 shows that the mean displacements are always  $\pm 3$  pixels in both directions at OP. 2 resulting in a low dynamic range. The points close to the optical access where discarded in PIV because of reflection from the wall and in LDV, since the flat face of the window brings flow disturbance inside the curve surface of the cone resulting in extra variance and bad data point.

The mean turbulence intensity profiles agree well in shape and in level except for OP. 1, where the CFD underestimated the intensity compared to the experiments. Another trend can be drawn from the figure: PIV measurements overestimate the rms level in all cases.



**FIGURE 7.** LDV, PIV and CFD turbulence intensity, OP. 1 to OP. 3, axis c

With both PIV and LDV, the velocity signals close to boundaries such as the shroud or the hub are more subject to noise from light reflection.

It is hard to have precise rms values with PIV measurement in hydraulic machinery flow since many factors may bring additional variance to the signal. For example, in this study we have distortion of the image from cone angle discontinuities and velocity gradients in the field that affect the accuracy. This influence is more pronounced in large spatial domains. The accuracy varies also depending on the position in the field, region with large curvature near the shroud are harder to get into focus even with the Scheimpflug condition. Loss of particle pairs may happen in some interrogation area, where  $C_t$  is large. Bad reflection of the light pulse on metallic components of the turbine might also occur but were avoided most of the time.

The turbulence intensity from the three components of the velocity is plotted for PIV in Fig. 9 and further conclusion are drawn about the large variance of the PIV signal. First, considering the LDV as the reference turbulence intensity level, the extra variance on PIV signal may come from the low radial velocity component, i.e., the particle displacement is so small in radial direction from two consecutive images that sub-pixel accuracy becomes an important error source (see bottom of Fig. 8). Sec-

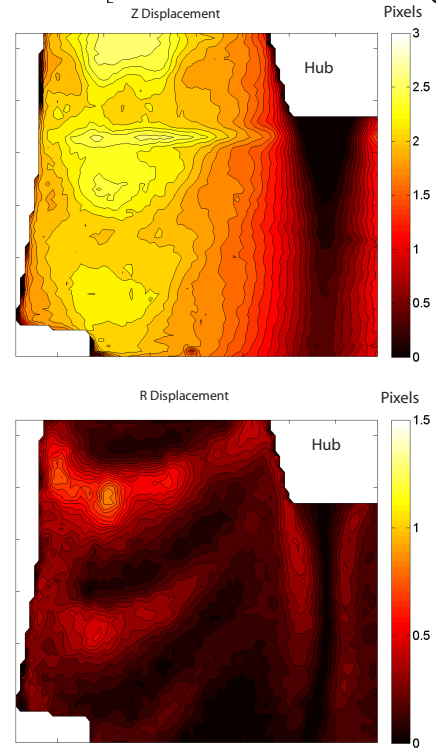


**FIGURE 8.** Z and R displacements of the particles in the PIV domain, OP. 2, 1 phase

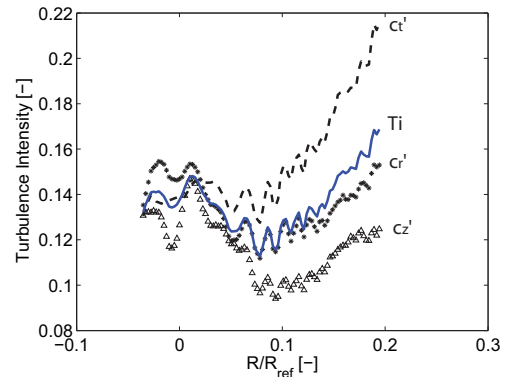


**FIGURE 9.** PIV turbulence intensity composition at OP. 3, axis c

ond, even though all precautions were taken to avoid loss of particles in the out of plane direction of the light sheet, it appeared in some interrogation area, often close to the wall in the tip vortex region. There is also additional variance to  $C_t$  since it is a result in the combination of the two camera fields with an image fit model. Gradient broadening effect in the PIV interrogation window of size  $\sim 11 \times 11 \text{ mm}^2$  are more stringent if compared with the LDV probe, where the longest measurement

volume dimension is around 5 mm in water with diameter around 0.2 mm.

It is hard to correct the above mention error sources even with uses of adaptative-correlation and median or range filters. It is presumed that a smaller spatial domain with better timing between images and longer particles displacement would lead to more precise rms values in this type of flow. There is therefore a trade off between the desired vector field size and the rms accuracy.

In numerical simulations, the transport equation for turbulence kinetic energy is mostly affected by the mesh and turbulence model type. Separation is known to be retarded with k-ε model and flow misalignment with the grid brings additional dissipation. Typical values of turbulence intensity expected at runner outlet for a Kaplan turbine lie around 10-20% (see e.g. [2]).

### Circumferential Non-Uniformity of the Flow

From LDV measurements, an integration of the axial component of the velocity,  $C_z$ , was performed over the radius for every azimuthal position and elevation b and c of the setup. Figure 10 illustrates the deviation from the reference flow,  $Q/Q_{ref}$ , represented by a plane on axis b and c. Planes were drawn by fitting the 6 integral values of the deviation obtained on the 6 half axis with a surface equation  $z = ax + by + c$ .

The white mark on the surfaces shows the vector pointing in the minimum flow deviation direction. A deviation of  $\pm 4\%$  is seen on the top figure for partial discharge operation (OP. 1). For the other regimes, the non-uniform flow lies around  $\pm 6\%$  of deviation. The swirl rate, S, is an indication of the swirl intensity of the main flow. It represents the ratio of the circumferential momentum flux to the axial momentum flux times the external radius of the channel:

$$S = \frac{\int_{R_0}^{R_1} 2\pi\rho C_t C_z R^2 dR}{R_1 \int_{R_0}^{R_1} 2\pi\rho C_z^2 R dR} \quad (5)$$

Values of S are computed with Eqn. 5 on the top left of Fig. 10. The non-uniformity of the flow cannot be sustained in a straight vertical position but rather follows a helicoidal path from the rotation of the mean flow relative to the momentum ratio value. At OP.2 and OP.3, the swirl rate is close to 0 and the main flow rotates in a clock-wise direction. One should note that in all cases, the non-uniformity tends to dissipate, i.e., the deviation at axis c is lower than at b. That indicates, the origin of the non-uniformity may occur upstream in the distributor and spiral casing of the turbine.

Previous analysis of the flow in the two admission channels of the turbine with CFD and LDV reveals around 15 % of difference in the mass flow rate between the channels. This difference

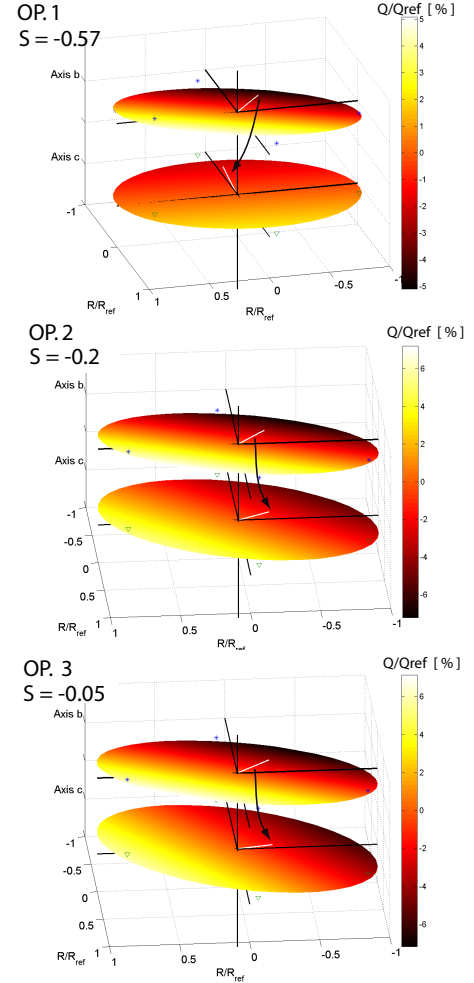


**FIGURE 10.** Circumferential non-uniformity of the flow for all OP. computed from LDV measurements

generates a strong shear flow downstream the admission pile and at the spiral casing tong that is transported downstream. It is unsure whether it is the pile or the tong that generates most of the non-uniformity. Insight from simulations tells us the admission tong is probably the main actor but it is to be confirmed since the large dissipation makes it hard to follow the non-uniformity pass the runner. In any case, the disturbance acts as one big wake on the runner blade and is transported by the runner rotation downstream. This phenomenon was also noticed in [3, 4].

To conclude this section, we remind that our main goal is to focus on the draft tube inlet flow. As we see, we must consider the whole turbine to explain flow phenomena at this location. This stresses the requirement to do complete machine simulations to better represent the flow of the draft tube inlet. It also shows that measurements at only one circumferential position cannot capture this type of flow phenomena.

It is easy to be misled with the periodic, quasi-inviscid flow

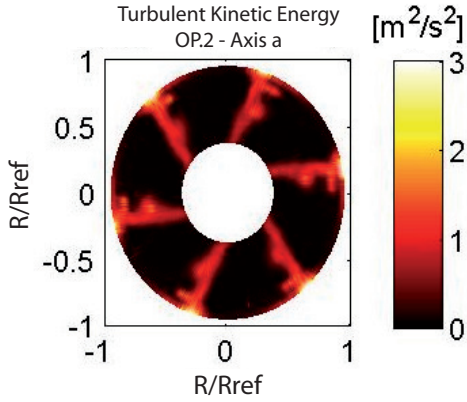


**FIGURE 11.** Inviscid and wake region exposed with the LDV phase resolved turbulent kinetic energy, OP.2, axis a

just after the runner when looking at the phase average profile on only one axis (Fig. 11). A figure like this allows the use of an axisymmetric profile with an averaged turbulence kinetic energy level for draft tube simulations without concern about non-uniformity. Except for energetic wake regions, the core flow is almost inviscid everywhere. The influence and consequences of such assumptions will be demonstrated briefly later on.

### Frequency analysis from LDV and CFD velocity signals

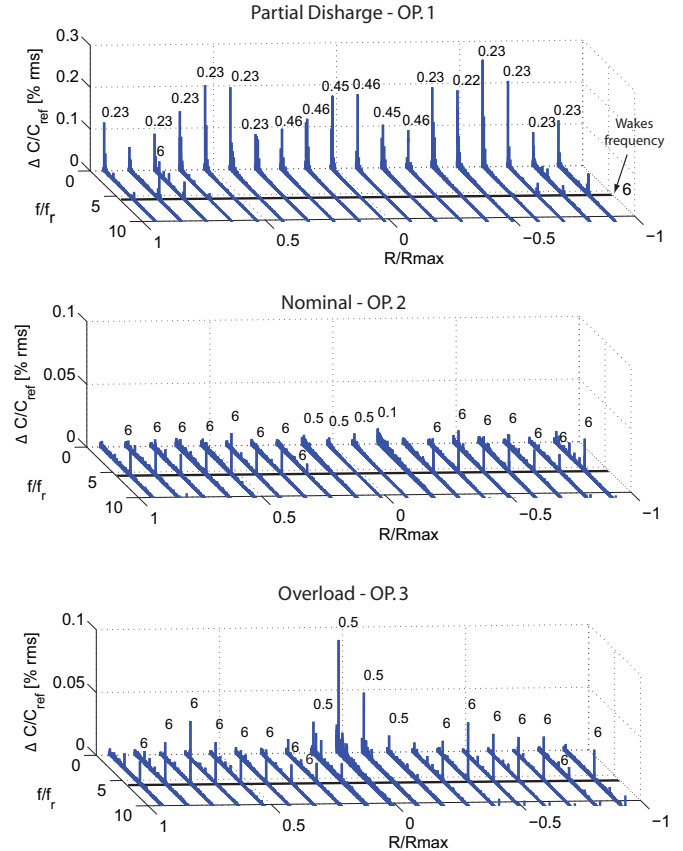
The spectrum of the velocity signal contains much information about flow fluctuations and phenomena at the draft tube inlet. In this section, we present the spectrum from the LDV velocity signals lying in the stationary reference frame. The random nature of particle arrival in the measurement volume of the LDV requires the use of special techniques such as a Lomb algorithm or sample and hold interpolation to perform FFTs.

Figure 12 shows a waterfall diagram of LDV spectra at elevation b and for each operating point. The maximum normalised frequency values are indicated on top of each spectral peak.

For all operating point, the blade passing frequency is clearly visible at 6 times the runner frequency,  $f_r$ . That is expected from the 6 runner blade wakes inducing a velocity deficit on the measuring volume of the LDV.

### Investigation of nominal and overload condition

On the two bottom illustrations, there are characteristic frequencies of  $0.5f_r$  appearing close to the hub, in the range  $-0.2 \lesssim R/R_{max} \lesssim 0.2$ . This phenomenon is much more intense at overload condition (OP.3), where fluctuations reach almost 10% of  $C_{ref}$  in the center. This suggest a similar behavior as the axial pulsating vortex rope seen in cavitation test at overload condition, where the low swirl number enforce axial fluctuations below the hub. Evidence of this phenomena are still to be confirm



**FIGURE 12.** Normalised frequency for all OP. from LDV measurements at axis b, azimuth  $93.5^\circ$

for our case but assuming the whole flow system adopts the easiest configuration, the hypothesis that a separation followed by a recirculation would pulse below the hub at a harmonic frequency of the runner at nominal and overload condition is worth mentioning.

Unsteady simulations, case 3, were performed at nominal head with two types of inflow conditions. The effect of the recirculation zone can be seen on the draft tube shown on Fig. 13. Both simulations show a large zone of recirculation in the channels. But the left figure expose a recirculation zone just below the runner that is not present in case 3.b on the right. Without detailing the boundary condition profile, a higher swirl intensity and a more uniform axial velocity profile in case 3.a is suspected to result in this type of recirculation [5]. For case 3.b, there is a mechanism that reenergizes the hub boundary layer and retard the separation.

Axial velocity profiles for OP.2 evidence a recirculation zone size inbetween cases 3 simulations (Fig. 14). There are no recirculation seen at elevation c of the experiments and URANS CFD case 2 of the bottom figure.



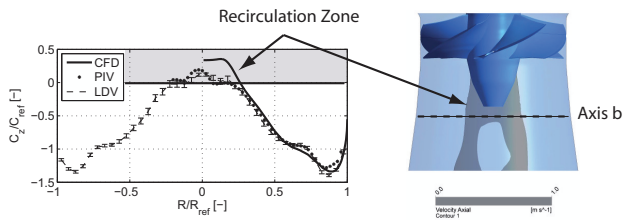


**FIGURE 17.** (Left) PIV, LDV and CFD axial velocity profile at axis b, OP. 1, (Right) Recirculation zone from CFD data, OP.1

combined with the error on the estimation of the FFT with the few runner rotations available for the URANS simulations. This is also why the signal had to be band-pass filtered.

The recirculation at partial discharge below the hub is shown for both URANS results and experiments on Fig. 17.

## Conclusion

The draft tube inlet flow was extensively studied with LDV, PIV and numerical simulations. The combination of experimental and numerical data gave much insight about the flow phenomena at draft tube inlet. That will in turn be of great help for further numerical studies to better define inlet boundary conditions for draft tube simulations.

## ACKNOWLEDGMENT

The authors would like to thank the participants on the Consortium on Hydraulic Machines for their support and contribution to this research project: Alstom Hydro Canada Inc., Andritz Hydro Ltd., Edelca, Hydro-Quebec, Laval University, NRCan, Voith Hydro Inc. Our gratitude goes as well to the Canadian Natural Sciences and Engineering Research Council who provided funding for this research.

## REFERENCES

- [1] Westerweel, J., and Scarano, F., 2005. "Universal outlier detection for piv data". *Experiments in Fluids*, **39**(6), pp. 1096–1100.
- [2] Andersson, U., 2009. "An experimental study of the flow in a sharp-heel kaplan draft tube". PhD thesis, Lulea University of Technology.
- [3] Castorph, D., and Raabe, J., 1974. "Measurement of unsteady pressure unsteady relative velocity field of a kaplan runner by means of an electronic multi-miniature probe as a basic contribution to research on unsteady runner load". In Proceedings of the 7 th IAHR Symposium.
- [4] Raabe, J., 1985. *Hydro Power: the design, use, and func-*

*tion of hydromechanical, hydraulic, and electrical equipment.* VDI-Verlag GmbH, Düsseldorf.

- [5] Skotak, A., and Obrovsky, J., October 24 - 26, 2007. "Low swirl flow separation in a kaplan turbine draft tube". In 2nd IAHR International Meeting of the Workgroup on Cavitation and Dynamic Problems in Hydraulic Machinery and Systems.
- [6] Skotak, A., Mikulasek, J., and Lhototakova, L., September 9 - 12, 2002. "Effect of the inflow conditions on the unsteady draft tube flow". In Proceedings of the XXIst IAHR Symposium on Hydraulic Machinery and Systems.